Contents lists available at ScienceDirect

Transactions of Nonferrous Metals Society of China

36(2026) 943−955

www.tnmsc.cn

Three-dimensional inversion of metallic minerals electromagnetic data using efficient multigrid solver

Yong-fei WANG [a], Rong-wen GUO [b,c,d,e], Zhuo LIU [f,*], Ding-hui YANG [a], Deng-kang WANG [b,c,d,e]

[a] Department of Mathematical Sciences, Tsinghua University, Beijing 100084, China;
[b] State Key Laboratory of Critical Mineral Research and Exploration, Central South University, Changsha 410083, China;
[c] School of Geosciences and Info-Physics, Central South University, Changsha 410083, China;
[d] Hunan Key Laboratory of Non-ferrous Resources and Geological Hazard Detection, Changsha 410083, China;
[e] Key Laboratory of Metallogenic Prediction of Nonferrous Metals and Geological Environment Monitoring, Ministry of Education, Central South University, Changsha 410083, China;
[f] Doerr School of Sustainability, Department of Earth and Planetary Sciences, Stanford University, Stanford, California 94305, USA

Abstract: A three-dimensional (3D) electromagnetic (EM) inversion algorithm based on the nonlinear conjugate gradient (NLCG) method and a two-color plane Gauss−Seidel (GS) multigrid (MG) forward solver is developed to improve inversion efficiency. The results indicate that the computational efficiency of each inversion can be improved by approximately a factor of three by using the proposed MG solver. First, the accuracy of the MG solver is validated through a test on a synthetic model. Next, the numerical performance of the inversion algorithm is evaluated using this model. Finally, the inversion algorithm is applied to a field EM data collected at the Beiya gold polymetallic ore district. A 3D resistivity model is obtained, and the formation process of the metal ore is analyzed.

Keywords: metallic minerals; electromagnetic data; gradient inversion method; multigrid solver

1 Introduction

Mineral resources are vital for national economic development and sustainable growth. Understanding metallogenic processes, deep material sources, and migration pathways improves resource potential assessments [1−3]. Electromagnetic (EM) methods [4] have been widely used in resource exploration [5−7]. 3D EM inversion provides more detailed and accurate structural information compared to 1D and 2D inversions. However, one major challenge of 3D inversion is the high computational cost regarding memory usage and computation time [4], which significantly limits its broader application.

The inversion of EM data requires accurate and efficient forward modeling [8], which can be achieved through using the integral equation method (IEM) [9], the finite element method (FEM) [10−12], the finite volume method (FVM) [13,14], and the finite difference method (FDM) [15]. These advancements lay the foundation for EM inversion [16,17]. The inverse problem is essentially an optimization problem, necessitating the use of an appropriate optimization algorithm. At present, the predominant gradient-based inversion methods include the Gauss−Newton (GN) method [17,18], the OCCAM method [19], the quasi-Newton (QN) method [20,21], and the nonlinear conjugate gradient

Corresponding author: *Zhuo LIU, Tel: +86-15084998048, E-mail: zliu93@stanford.edu
https://doi.org/10.1016/S1003-6326(25)67008-7
Received 23 May 2025; accepted 28 January 2026

(NLCG) method [22,23]. Unlike other methods, the NLCG does not require direct storage of the Jacobian matrix. Instead, it only computes the product of the Jacobian matrix and a vector through "adjoint forward modeling" during the inversion process, thereby significantly reducing memory usage [24,25]. This advantage makes NLCG particularly effective for large-scale 3D EM data inversions and it is currently one of the most widely used methods for such applications [15].

In the field of 3D EM inversion, a major bottleneck that still needs to be overcome is that conventional inversion methods often yield overly diffuse resistivity models, which severely compromise the accuracy of the geological interpretation. Furthermore, the vast model space inherent in 3D inversion not only exacerbates the issue of non-uniqueness but also significantly increases computational complexity. To address these challenges, CAI et al [26] pioneered the 3D multinary inversion method for controlled-source EM data, which integrates various rock physics priors to construct multinary transformation functions. This approach enables precise delineation of resistivity boundaries, significantly enhancing both model resolution and the reliability of geological interpretation. Building on this, WANG et al [27] further advanced the field by proposing a novel 3D EM inversion method based on sub-domain decomposition and minimum entropy constraints. This technique not only achieves higher-resolution resistivity models via minimum entropy constraints, but also effectively reduces the dimensionality of the model parameters through sub-domain decomposition, thereby substantially improving computational efficiency and alleviating the resolution artifacts caused by excessive forward-model grid refinement.

In recent years, several efficient 3D EM inversion packages have been developed based on these forward modeling and inversion methods, such as jif3D [28], WSINV3DMT [29], AP3DMT [30], DEVA3DMT [31] and ModEM [32]. Among them, ModEM, which is based on FDM, has gained particularly widespread attention and application [33]. However, all of the above-mentioned inversion packages above still requires significant computational resources when applied to large-scale survey datasets. The most time-consuming aspect of each inversion iteration is the forward and adjoint modeling. Consequently, numerous studies have sought to accelerate 3D EM forward modeling [34], including divergence correction schemes [35], multi-resolution sampling [36], regularization technique [37,38], and decomposing EM fields into potentials [39]. However, these techniques often involve computational costs that increase nonlinearly with the number of degrees of freedom.

The multigrid (MG) solver [40], has recently garnered significant attention in geophysical applications due to its excellent convergence properties [41−44] and the computational time scales linearly with the number of grid size. The MG solver can be used as a stand-alone solver [45] or a preconditioner for Krylov subspace solvers [46] in the forward modeling. However, little knowledge on their numerical performance in inversion is documented in the literature, and the benefit of incorporating the MG algorithm in inversion has not been explored.

In this study, we implement a NLCG inversion scheme based on a two-color plane Gauss−Seidel (GS) MG solver [40]. During the implementation process, the benefits of incorporating our MG algorithm in NLCG has been demonstrated. A synthetic dataset is used to assess the numerical performance of the inversion algorithm with ModEM serving as the benchmark. After confirming the accuracy and efficiency of our algorithm, a field EM dataset is used to evaluate the practical efficacy of this algorithm for probing deep structures.

2 Electromagnetic forward modeling

For natural source EM surveys, the displacement currents are typically negligible. An $e^{-i\omega t}$ time dependence is assumed, and SI units are used. According to Maxwell's equations and assuming the elimination of the magnetic fields $\boldsymbol{H}$, the electric fields $\boldsymbol{E}$ can be written as

$$\nabla\times\nabla\times\boldsymbol{E}-i\omega\mu_0\sigma\boldsymbol{E}=0 \tag{1}$$

where $i=\sqrt{-1}$, and ω, μ_0 and σ denote the angular frequency, the magnetic permeability, and the electrical conductivity, respectively. Equation (1) can be solved by either direct or iterative solvers with appropriate boundary conditions. Then, the secondary magnetic field can be calculated from:

$$\boldsymbol{H}=(-i\omega\mu_0)^{-1}\nabla\times\boldsymbol{E} \tag{2}$$

2.1 Discretization

To solve Eq. (1), we need to discretize the equation commonly using either FDM or FEM [31]. In this study, FDM [15] is used to discretize Eq. (1) on staggered grids, with the electrical components defined on cell edges and magnetic components on cell faces (see Fig. 1). The discretized form of Eq. (1) can be written as

$$[\boldsymbol{C}^{\dagger}\boldsymbol{C}-\mathbf{diag}(\mathrm{i}\omega\mu_0\sigma_{\mathrm{e}})]\boldsymbol{e}=\boldsymbol{0} \tag{3}$$

where **diag** denotes a diagonal matrix, and σ_{e} is the edge conductivity averaged from four cells surrounding the edge; $\boldsymbol{C}$ is the discrete curl operator mapping the cell edge components to the cell faces, and $\boldsymbol{C}^{\dagger}$ is the adjoint of $\boldsymbol{C}$, mapping back to interior cell edges (see Ref. [15]). The Eq. (3) can be expressed in matrix form as

$$\boldsymbol{A}\boldsymbol{e}=\boldsymbol{b} \tag{4}$$

where $\boldsymbol{A}$ is the coefficients assembled from all elements, $\boldsymbol{e}$ is the discrete electrical fields, and $\boldsymbol{b}$ is the vector, incorporating both source terms and boundary conditions.

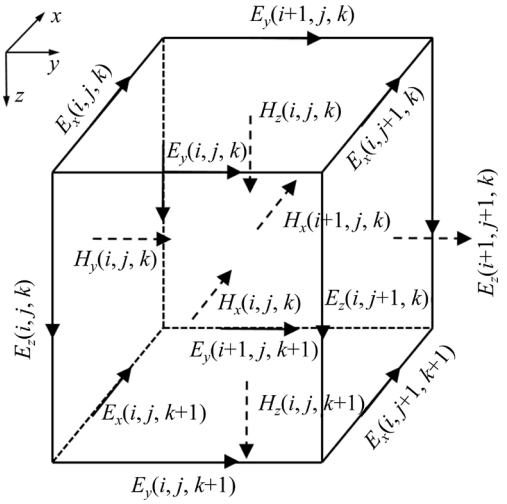

Fig. 1 Staggered FD discretization for 3D EM forward problems

2.2 Multigrid solver

MG methods first remove short-range errors via fine-grid smoothing operations, and then project residual long-range errors onto coarser grids. These long-range errors are then solved inexpensively on the coarsest grid, and the solutions are interpolated sequentially back to the finest grid to correct the solutions (Fig. 2). The transitions between the finest and the coarsest grids can follow either V-cycle, W-cycle or F-cycle (Fig. 3). To implement MG, multiple components are required, including coarse-grid operators, restriction and prolongation operators, and the smoother [40]. For natural source EM forward modeling problems, the abundant null spaces of the curl−curl equations cause slow convergence or even divergence of the MG method at long periods. This issue can be addressed by using cellblock GS smoother [42], which is based on domain decomposition. Recent studies show that the line GS or plane GS smoothers can improve the ability of MG solvers to handling grid stretching [45,46]. In this study, we adopt the MG with two color-plane GS smoother (Fig. 4) proposed by WANG et al [40] to solve the forward modeling problems and its adjoint problems in the inversion. Note that the small discrete equation for the unknown components (red arrows in Fig. 4(a)) defined in a given region can be efficiently solved using LU decomposition, with the surrounding boundary conditions (gray arrows in Fig. 4(a)) having values obtained from previous iterations.

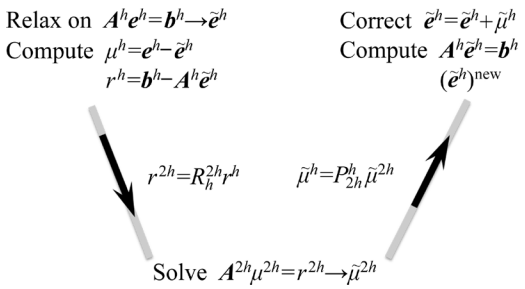

Fig. 2 Diagram of process of MG method

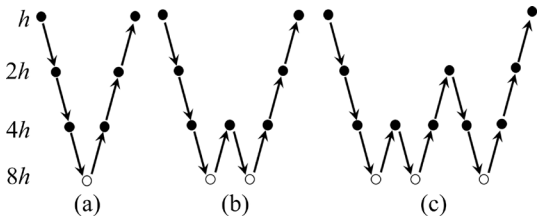

Fig. 3 Transitions between finest and coarsest grids: (a) V-cycle; (b) W-cycle; (c) F-cycle

For the two color-plane GS smoother, we first group all the planes into two colors, with the only requirement that any two plane systems in each color should be disjoint (see Fig. 4(b)). Thus, the system for each plane with the same color can be distributed to different machines and solved in parallel. The parallel implementation in the code is based on OpenMP, with more detailed treatment provided in Ref. [8].

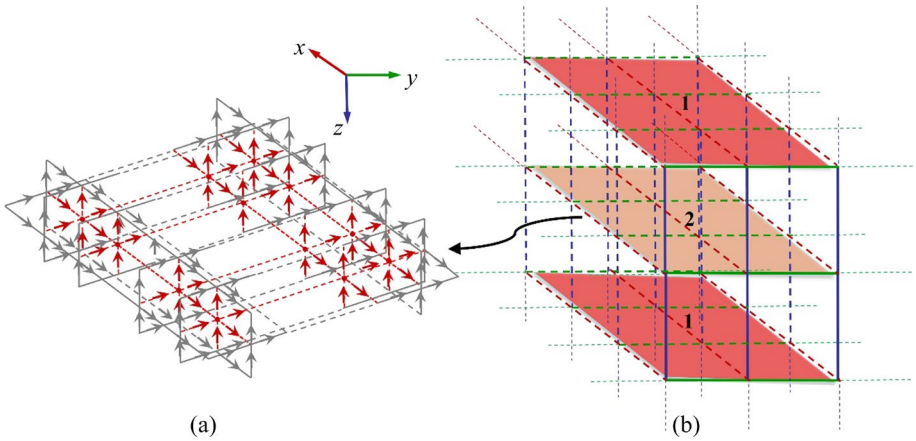

Fig. 4 Diagram of two-color plane GS smoother: (a) One plane system; (b) Two color plane system

3 Inversion theory

The purpose of 3D EM inversion is to develop a mathematical framework that transforms the information contained in the observed data space to the model space, in order to recover the model, reproducing most of the observations. According to Ref. [29], the objective function of 3D EM inversion can be defined as

$$\Phi(\boldsymbol{m},\boldsymbol{d})=(\boldsymbol{d}-\boldsymbol{F}(\boldsymbol{m}))^{\mathrm{T}}\boldsymbol{C}_{\mathrm{d}}^{-1}(\boldsymbol{d}-\boldsymbol{F}(\boldsymbol{m}))+\lambda(\boldsymbol{m}-\boldsymbol{m}_0)^{\mathrm{T}}\boldsymbol{C}_{\mathrm{m}}^{-1}(\boldsymbol{m}-\boldsymbol{m}_0) \tag{5}$$

where λ is the regularization factor; $\boldsymbol{d}$ is the observed data; The forward operator, $\boldsymbol{F}(\boldsymbol{m})$, denotes predicted data from the model $\boldsymbol{m}$; $\boldsymbol{m}_0$ is the reference model and $\boldsymbol{C}_{\mathrm{m}}$ is the model covariance matrix; $\boldsymbol{C}_{\mathrm{d}}$ is the data covariance matrix, given by

$$\boldsymbol{C}_{\mathrm{d}}^{-1}=\mathbf{diag}\left\{1/\delta_1^2,\ 1/\delta_2^2,\ \cdots,\ 1/\delta_N^2\right\} \tag{6}$$

where δ is the standard deviation for the observed data.

According to Ref. [15], Eq. (5) can be more concisely reformulated into

$$\Phi(\tilde{\boldsymbol{m}},\boldsymbol{d})=[\boldsymbol{d}-\tilde{\boldsymbol{F}}(\tilde{\boldsymbol{m}})]^{\mathrm{T}}[\boldsymbol{d}-\tilde{\boldsymbol{F}}(\tilde{\boldsymbol{m}})]+\lambda\tilde{\boldsymbol{m}}^{\mathrm{T}}\tilde{\boldsymbol{m}}=\|\boldsymbol{d}-\tilde{\boldsymbol{F}}(\tilde{\boldsymbol{m}})\|^2+\lambda\|\tilde{\boldsymbol{m}}\|^2 \tag{7}$$

where $\tilde{\boldsymbol{m}}=\boldsymbol{C}_{\mathrm{m}}^{-1/2}(\boldsymbol{m}-\boldsymbol{m}_0)$, and $\tilde{\boldsymbol{F}}(\tilde{\boldsymbol{m}})=\boldsymbol{F}(\boldsymbol{C}_{\mathrm{m}}^{1/2}\tilde{\boldsymbol{m}}+\boldsymbol{m}_0)$. The inversion solution can be obtained by searching for a solution that minimizes Eq. (7). The searching process is typically based on either the GN method or NLCG method based on the linearization of $\tilde{\boldsymbol{F}}(\tilde{\boldsymbol{m}})$. In this study, NLCG is applied directly to minimize Eq. (7). Following the work of Ref. [15], NLCG needs to calculate the gradient, the derivative of Eq. (7) with respect to $\boldsymbol{m}$ at m_n as

$$\left.\frac{\partial\Phi}{\partial\boldsymbol{m}}\right|_{m_n}=-2\boldsymbol{J}^{\mathrm{T}}(\boldsymbol{d}-\boldsymbol{F}(m_n))+2\lambda m_n \tag{8}$$

where $\boldsymbol{J}$ is the Jacobian (sensitivity) matrix with entries, given by

$$J_{jk}=\frac{\partial F_j(\boldsymbol{m})}{\partial m_k} \tag{9}$$

Assuming that the forward operator is a function of the discrete electric fields $\boldsymbol{e}$ and model $\boldsymbol{m}$, we have

$$F_j(\boldsymbol{m})=\psi_j(\boldsymbol{e}(\boldsymbol{m}),\boldsymbol{m}) \tag{10}$$

where ψ_j is commonly a nonlinear function.

According to the chain rule, Eq. (9) can be calculated by

$$J_{jk}=\frac{\partial\psi_j(\boldsymbol{e}(\boldsymbol{m}),\boldsymbol{m})}{\partial m_k}=\sum_l\frac{\partial\psi_j}{\partial e_l}\frac{\partial e_l}{\partial m_k}+\frac{\partial\psi_j}{\partial m_k} \tag{11}$$

where l represents the number of discrete electric fields $\boldsymbol{e}$ included in ψ_j.

The Eq. (11) can be rewritten in matrix form as

$$\boldsymbol{J}=\boldsymbol{L}\boldsymbol{F}+\boldsymbol{Q} \tag{12}$$

where $\boldsymbol{L}$ is a linearized functional matrix, and $\boldsymbol{Q}$ is the matrix containing the functional derivative with respect to the model $\boldsymbol{m}$.

The $\boldsymbol{F}$ represents the model derivative of discrete electric fields $\boldsymbol{e}$, given by

$$\boldsymbol{F}=\boldsymbol{A}_{m_0}^{-1}\boldsymbol{P} \tag{13}$$

where $\boldsymbol{P}=\left.\frac{\partial(\boldsymbol{A}\boldsymbol{e}_{m_0})}{\partial\boldsymbol{m}}\right|_{m_0}$ and $\boldsymbol{e}_{m_0}$ is the solution of

Eq. (4) at m_0. We assume that the coefficient matrix for m_0 is $\boldsymbol{A}_{m_0}$.

Substituting Eq. (13) into Eq. (12), we have

$$\boldsymbol{J}=\boldsymbol{L}\boldsymbol{A}_{m_0}^{-1}\boldsymbol{P}+\boldsymbol{Q} \tag{14}$$

where $\boldsymbol{P}$ depends on details of both the numerical modeling implementation and the conductivity parametrization.

In Eq. (8), we need to calculate the transpose of $\boldsymbol{J}$ as

$$\boldsymbol{J}^{\mathrm{T}}=\boldsymbol{P}^{\mathrm{T}}(\boldsymbol{A}_{m0}^{\mathrm{T}})^{-1}\boldsymbol{L}^{\mathrm{T}} \tag{15}$$

We assume $\boldsymbol{r}=\boldsymbol{d}-\boldsymbol{F}(m_n)$, and the computation of $\boldsymbol{J}^{\mathrm{T}}\boldsymbol{r}$ is only required without explicit calculation of $\boldsymbol{J}$. Thus, substituting Eq. (15) into the misfit term in Eq. (8), the inverse of $\boldsymbol{A}_{m_0}^{\mathrm{T}}$ can be considered as a solution process for the following equation, defined by

$$\boldsymbol{A}_{m}^{\mathrm{T}}\boldsymbol{e}_{\mathrm{adj}}=\boldsymbol{L}^{\mathrm{T}}\boldsymbol{r} \tag{16}$$

For NLCG, each iteration typically requires two forward modeling calculations and one adjoint solution as indicated in Fig. 5. In this study, both the adjoint (Eq. (16)) and forward modeling are solved by MG with the two color-plane GS smoother, and the LU decomposition results obtained during forward modeling calculation for one mode are stored and reused to solve the forward modeling for the remaining mode and their adjoint calculation.

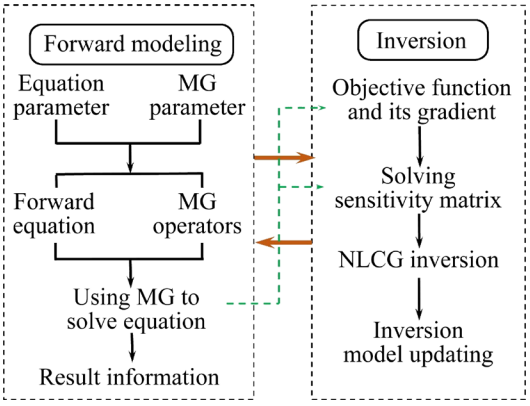

Fig. 5 Flowchart of MG for solving forward modeling problems and its adjoint problems

The NLCG inversion updates the model in a single iteration based on the search direction and the search step size [47]. The search direction, which commonly begins as a negative gradient, is chosen to minimize the objective function, and the search size indicates the distance moved in the search direction. Further information about NLCG can be found in Ref. [32].

4 Synthetic inversion tests

The synthetic model is made up of a 100 Ω·m half space with six embedded anomalies with resistivities of 10 Ω·m and 1000 Ω·m, respectively, as shown in Fig. 6. There are three shallow-buried anomalies with a size of 10 km × 10 km × 2 km, and the other three anomalies with a size of 10 km × 10 km × 10 km are located at a depth of 3 km. The total computational area (153 km × 153 km ×153 km) is uniformly discretized into 128 × 128 × 144 cells (with 16 air layers). Forward modeling is performed over eight logarithmic time periods ranging from 0.1 to 100 s. A total of 144 EM observation points, spaced 7 km apart are used. A 3% Gaussian random noise is added to the data, and the error floor is set to be 3% of $\sqrt{Z_{xy}\cdot Z_{yx}}$ for the impedance data and 0.03 for the tipper data. For MG solver, we employ a coarsening factor of (2, 2, 2) with 6 coarsening level and an F-cycle scheme. All tests in this study are run on an Intel Xeon Gold 6248R 3.0 GHz high-performance computer.

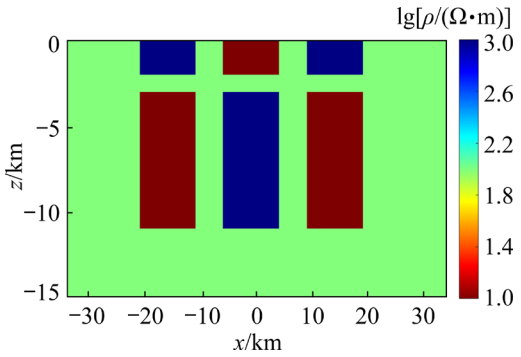

Fig. 6 Diagram of synthetic model with six blocks

With the BiCGstab solver preconditioned by BlockILU (referred to as BlockILU-BiCGstab, from ModEM) as the benchmark, we first examine the accuracy of this MG algorithm. The apparent resistivities and phases for x- and y-polarizations are both tested at a period of 10 s along a receiver line. The results in Fig. 7 demonstrate strong agreement between MG and BlockILU-BiCGstab solutions. The relative differences of apparent resistivities for ρ_{xy} and ρ_{yx} are respective 0.018% and 0.021% with

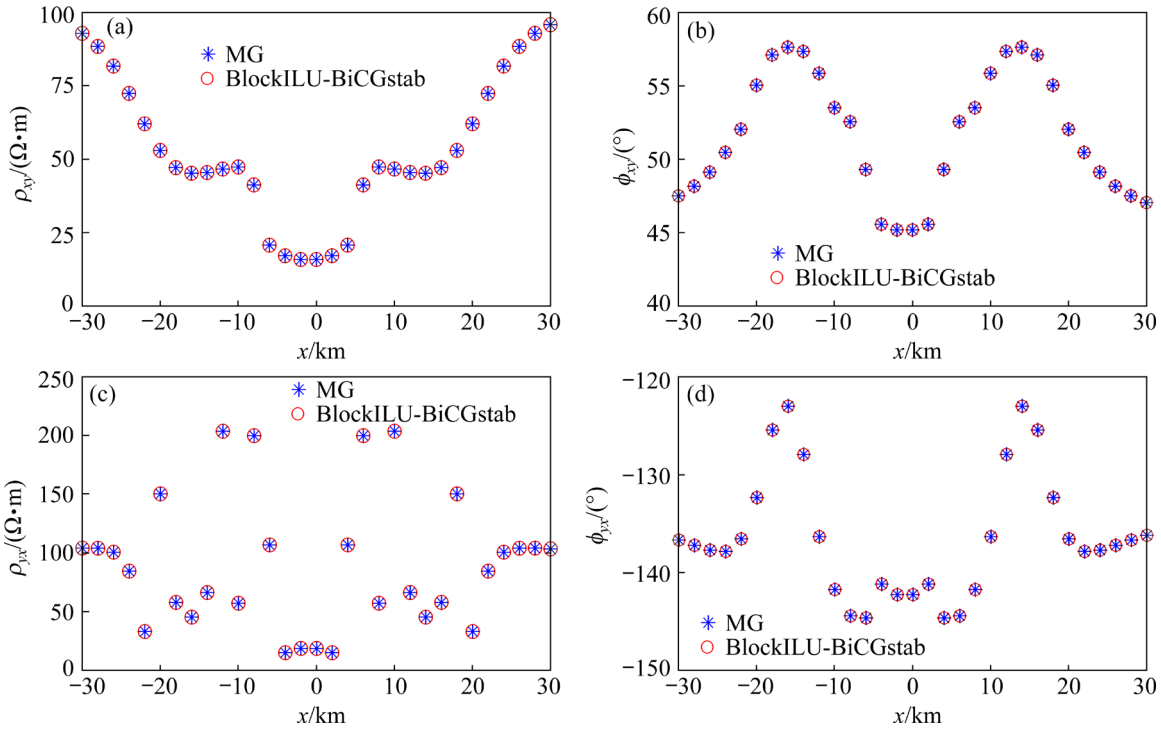

Fig. 7 Comparison of (a, c) apparent resistivity and (b, d) phase from MG and BlockILU-BiCGstab at period of 10 s along receiver line

phase differences of 0.00007° for ϕ_{xy} and 0.0001° for ϕ_{yx}, respectively.

Then, we examined the efficiency of the MG algorithm. Data at all eight periods ranging from 0.1 to 100 s are considered. For all periods, our MG outperforms BlockILU-BiCGstab with a reduction in computational time ranging from 69% to 89% (Table 1). Notably, the computational time of BlockILU-BiCGstab increases significantly as the period increases, which is typical for traditional Krylov subspace solvers. In contrast, the computational time of the MG varies slightly across all periods, showing good stability.

Table 1 Comparison of total computational time (sum of *x*- and *y*-polarizations) for MG and BlockILU-BiCGstab at different periods based on synthetic model discretized with grid of 128×128×144 cells

Period/s	Computational time/s		Reduction/%
	MG	BlockILU-BiCGstab	
0.01	131	425	69
0.037	128	508	75
0.139	127	565	77
0.518	127	620	79
1.931	128	800	84
7.197	126	859	85
26.827	129	885	85
100.0	122	1178	89

The inversion for the data was carried out by using our inversion code based on MG (called MG-inversion for convenience) and ModEM. ModEM inversion serves as a reference for evaluating the accuracy and efficiency of our MG-inversion. The inversion model is discretized into 128×128×128 cells with a uniform cell size of 1.2 km × 1.2 km × 0.6 km in the central region. The cell size is slightly stretched toward the boundaries horizontally while a vertical stretching factor of 1.25 is applied in the deeper region. Both the initial and reference models are uniform half-space with a resistivity of 100 Ω·m. The target RMS value is set at 1.05, with the regularization factor (λ) of 10 and the covariance value (α) of 0.3. After eight iterations, both methods achieved an RMS value less than 1.05 (1.01 for MG-inversion and 0.99 for ModEM) (Fig. 8) reduced from an initial RMS value of 3.56. While the inversion results show that both methods can effectively recover the position and shape of the anomaly, MG-inversion provides more precise

boundaries of anomalies (Fig. 9). The difference between the two methods is mainly reflected in the computational time. ModEM takes a total time of 42.27 h, while the MG-inversion takes 11.05 h, representing an acceleration ratio of 3.83. ModEM takes 4.85 h for each inversion iteration, while the MG-inversion takes only 1.28 h.

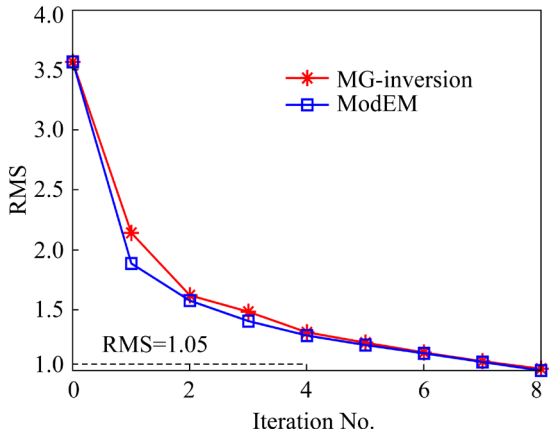

Fig. 8 Comparison of RMS convergence curves of MG-inversion and ModEM

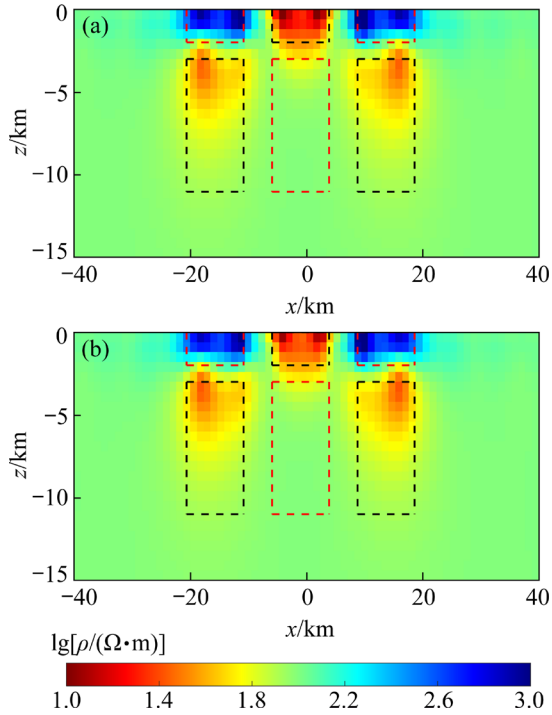

Fig. 9 Vertical slice of inversion results from (a) MG-inversion and (b) ModEM

5 EM data from Beiya gold polymetallic ore region

The Beiya gold polymetallic ore is one of the largest gold deposits in the world and one of the most representative deposits in the Jinshajiang−Ailaoshan alkali-rich porphyry belt [33]. During the Cenozoic, the Indian plate collided with the Eurasian plate, compressing and reorienting the elongated eastern margin of the Tibet continental block. Before the Eocene extrusion of this block, two significant porphyry-skarn ore groups were formed at the junction of the northern, middle, and southern sections of the Jinshajiang−Ailaoshan suture zone [48]. The Beiya polymetallic deposit, located in the middle part of this metallogenic belt, is generally believed to be closely related to alkaline porphyry intrusion. However, studies offer different perspectives on the tectonic genesis of these porphyries, with the prominent theories including (1) a strike-slip model [49], (2) a continental subduction model [50], and (3) a lithosphere delamination model [51].

To find out which theory fits best the actual formation process of these porphyries, we inverted the natural source EM data using the MG-inversion algorithm [33]. The dataset consists of 44 broadband EM stations covering the Beiya deposit (Fig. 10). The spacing between the stations varies from 5 to 20 km, and the data consist of 20 periods in the range of 0.003−1370 s.

According to Ref. [52], the phase tensor is an asymmetric tensor. Its fundamental characteristics can be represented using an ellipse, with parameters and a schematic diagram (Fig. 11) as follows:

$$\Phi_{\max}=\frac{1}{2}\sqrt{\left(\Phi_{xx}+\Phi_{yy}\right)^2+\left(\Phi_{xy}-\Phi_{yx}\right)^2}+\frac{1}{2}\sqrt{\left(\Phi_{xx}-\Phi_{yy}\right)^2+\left(\Phi_{xy}+\Phi_{yx}\right)^2} \tag{17}$$

$$\Phi_{\min}=\frac{1}{2}\sqrt{\left(\Phi_{xx}+\Phi_{yy}\right)^2+\left(\Phi_{xy}-\Phi_{yx}\right)^2}-\frac{1}{2}\sqrt{\left(\Phi_{xx}-\Phi_{yy}\right)^2+\left(\Phi_{xy}+\Phi_{yx}\right)^2} \tag{18}$$

$$\alpha=\frac{1}{2}\arctan^{-1}\left[\left(\Phi_{xy}+\Phi_{yx}\right)/\left(\Phi_{xx}-\Phi_{yy}\right)\right] \tag{19}$$

$$\beta=\frac{1}{2}\arctan^{-1}\left[\left(\Phi_{xy}-\Phi_{yx}\right)/\left(\Phi_{xx}+\Phi_{yy}\right)\right] \tag{20}$$

where $\Phi_{\max}$ and $\Phi_{\min}$ represent the major and minor axes of the ellipse, respectively, α denotes the structural strike angle, and β is the skew angle. In general, for 1D structures, $\Phi_{\max}=\Phi_{\min}$ (where the ellipse becomes a circle) and $\beta=0$; for 2D structures, the elliptical shape appears with $\beta=0$; while for 3D

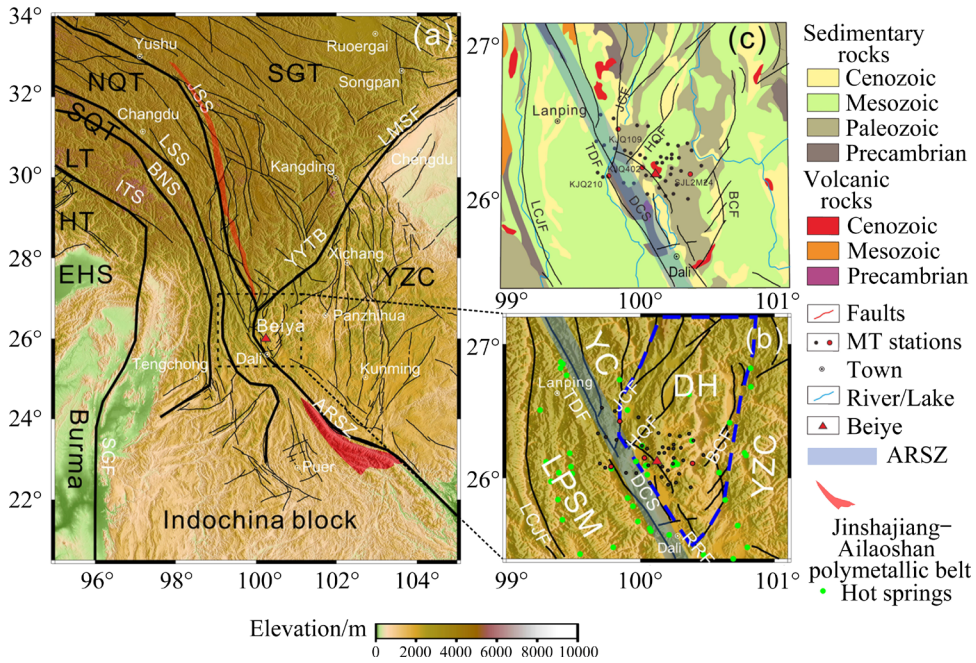

Fig. 10 Schematic map of geological structure and distribution of natural source EM stations around Beiya deposit (Modified from Ref. [33])

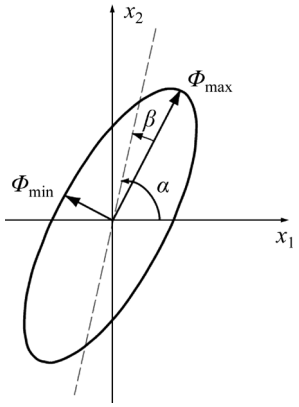

Fig. 11 Graphical representation of phase tensor (Redrawn from Ref. [52])

structures, $\beta \neq 0$, and the greater the deviation of β from 0, the stronger the 3D characteristics. In practical applications, cases where $|\beta|>3°$ are generally considered to represent 3D structures. The phase tensor ellipses at different periods are shown in Fig. 12. It can be seen that most stations exhibit strong 3D characteristics ($|\beta|>3°$), particularly for long periods.

5.1 Inversion parameter and results

In the inversion, the error floor is set as follows: for the impedance data, the error floors of Z_{xx} and Z_{yy} are $10\%\sqrt{|Z_{xy}\cdot Z_{yx}|}$, with $5\%\sqrt{|Z_{xy}\cdot Z_{yx}|}$ for Z_{xy} and Z_{yx}, while the error floor for tippers is 0.03. The computations were carried out on an Intel Xeon(R) Gold 6248R 3.0 GHz high-performance computing platform. The cycle mode and coarsening factor of MG are the same as before, while the coarsening level is 5.

The inversion area is 205 km × 205 km × 104 km, discretized into 64 × 64 × 64 cells, with the smallest cell size of 2 km × 2 km × 1 km in the central region. The cell size is slightly stretched toward the boundaries in the horizontal direction, with a stretching factor of 1.25 applied vertically in the deeper region. The initial model and reference model used in inversion are a uniform half-space with a resistivity of 100 Ω·m. The regularization factor is λ=0.1 and covariance value is α=0.1. The RMS decreases from 13.31 to 2.92 after 174 iterations. Figure 13 shows the final value of the RMS for each EM station. In general, the RMS value of most stations is less than 2, indicating a good fit for the data.

5.2 Geological interpretation and discussion

Three vertical slices were made along both the x direction (at x_1=−40 km, x_2=15 km, x_3=40 km) and the y direction (at y_1=−20 km, y_2=5 km, y_3=25 km), as shown in Fig. 14. The results indicate three major low-resistance bodies C1, C2 and C3. A large high-

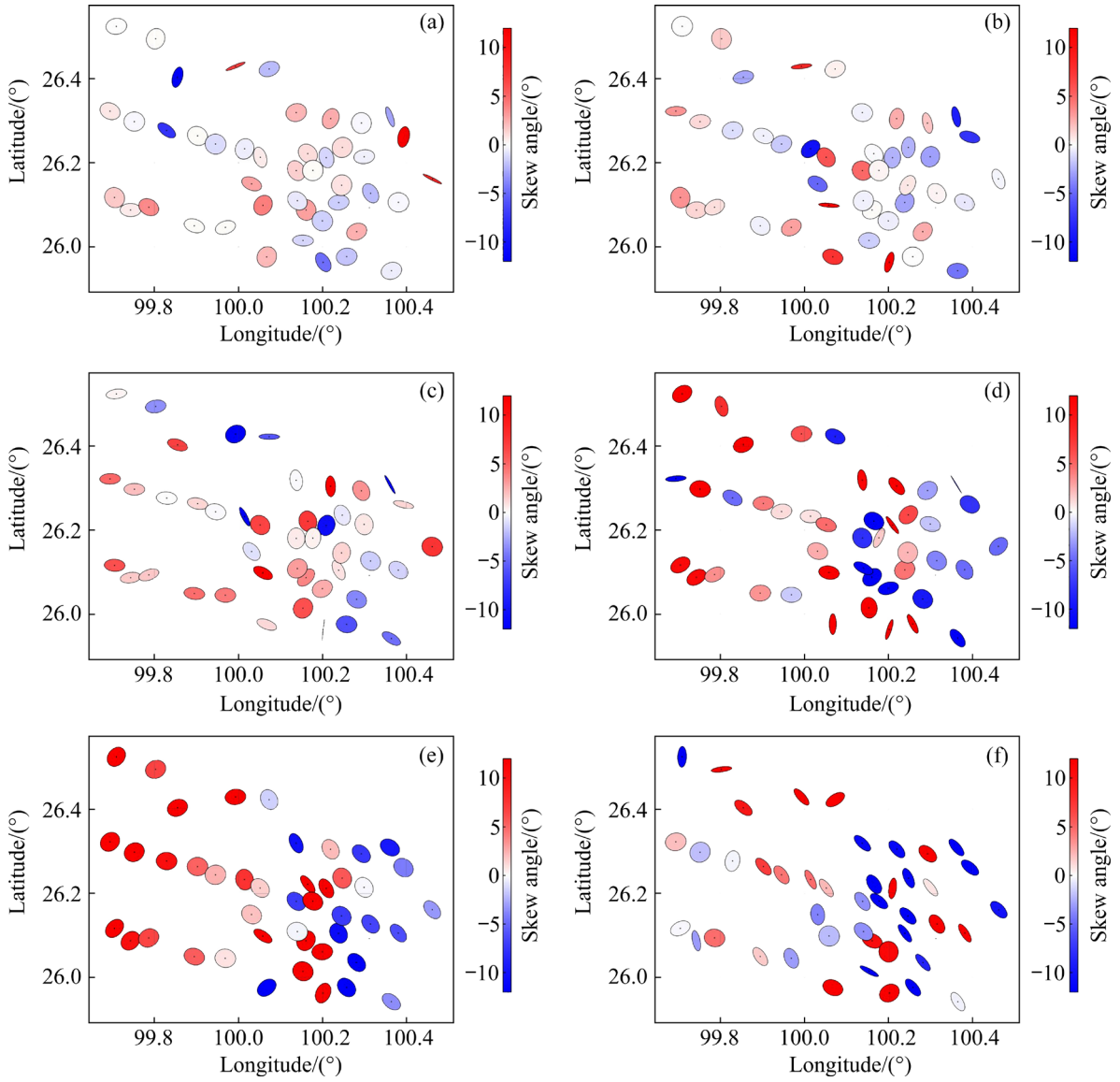

Fig. 12 Phase tensors for EM data at different periods: (a) 0.01 s; (b) 0.1 s; (c) 1 s; (d) 10 s; (e) 100 s; (f) 1000 s

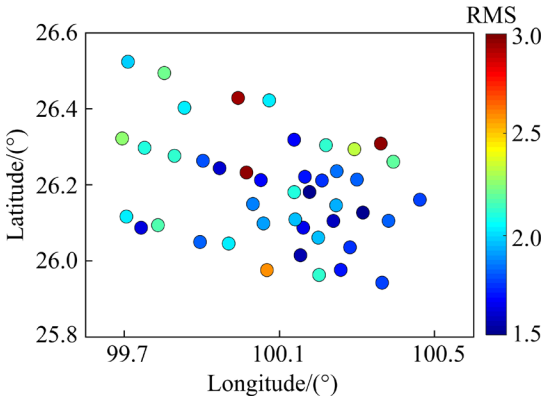

Fig. 13 RMS misfit of EM data for MG-inversion

resistance body overlies on C1. Both C1 and C2 extend from near the surface down to a depth of about 10 km. C1 and C2 are likely to be connected at a depth, as indicated in the y_2 slice.

Horizontal slices at different depths are shown in Fig. 15, indicating a similar structure to that obtained in Ref. [33]. It can be seen from Fig. 15 that there are low-resistance blocks at a depth of 5 km, surrounded by high-resistance blocks. At a depth of 10 km, the low-resistance blocks corresponding to C1, C2 and C3 can be seen. C3 is relatively small, and its formation may be linked to C2, as indicated in Fig. 14. At the depths of 20 and 30 km, it can be inferred that C2 and C3 have likely merged into a single block (Fig. 16), potentially representing upwelling channels of deep substances.

Combining the proposed model with the geological setting, the study area is located within the Ailaoshan−Honghe shear zone, and various

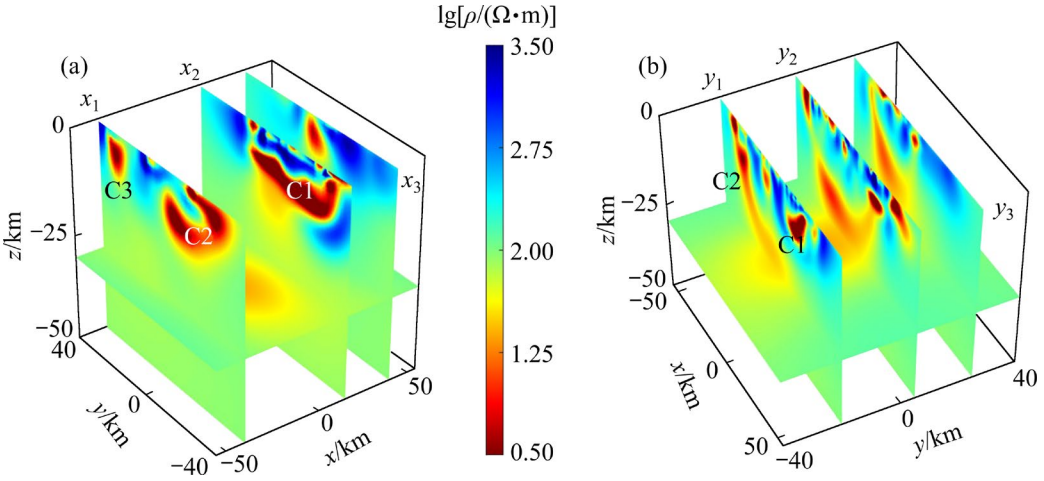

Fig. 14 3D inversion resistivity model of Beiya deposit: (a) *y*–*z* slice view; (b) *x*–*z* slice view

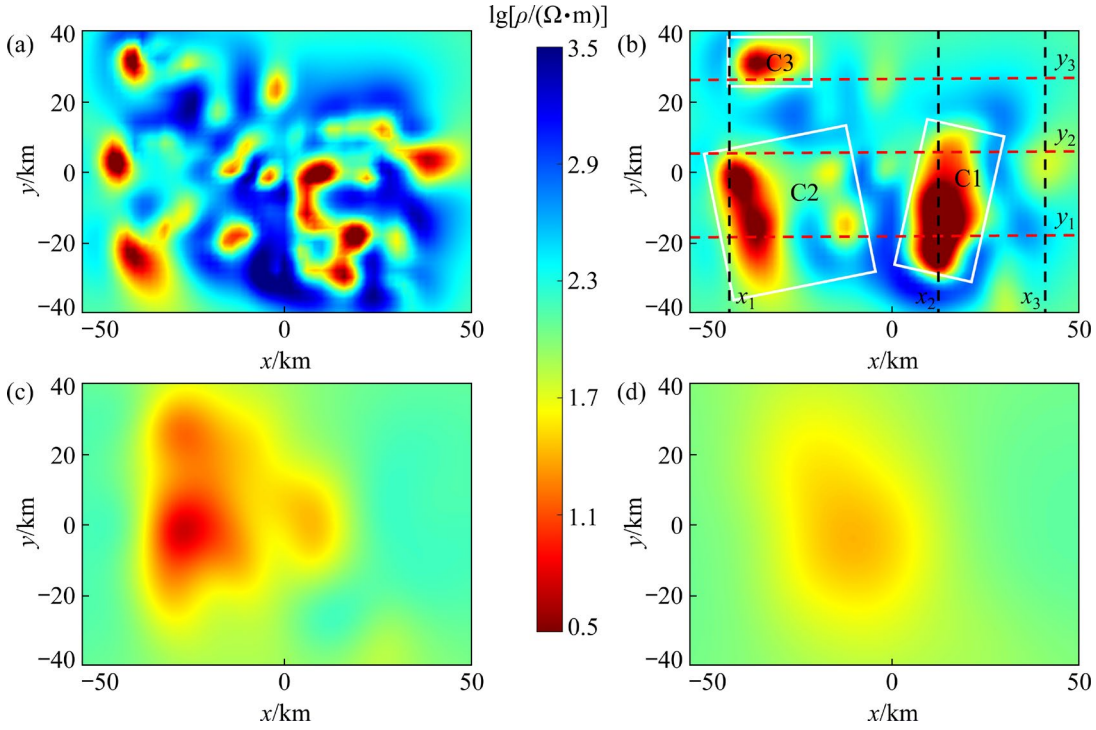

Fig. 15 Horizontal slice of inversion results at different depths: (a) 5 km; (b) 10 km; (c) 20 km; (d) 30 km

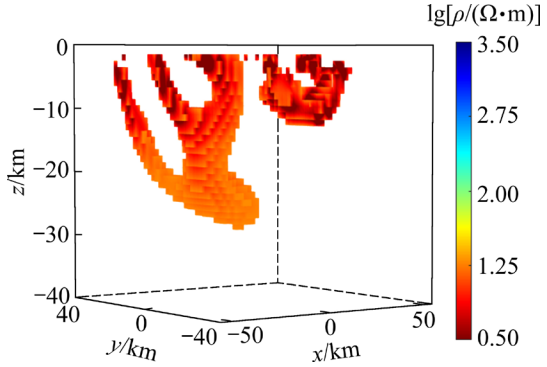

Fig. 16 3D view of low-resistance bodies in inversion results

interpretations exist for the low-resistance body (C2) below the shear zone, including the presence of metal sulfide minerals, graphite, saline fluids, structural water, and molten materials. YU et al [33] interpreted C2 as structural water and partial melting associated with the shear zone. In contrast, C1 is interpreted as metal sulfide and saline fluids, corresponding to an ancient magma chamber (with the Beiya polymetallic deposit located above C1). The high-resistivity body above C1 acts as a good reservoir. Our results suggest that the Beiya polymetallic deposit was formed in association with

the Ailaoshan−Honghe shear zone, where the volatile, metal-rich fluids from the ancient magma chamber rise further through the Ailaoshan−Honghe fault system, becoming the metal source for Beiya polymetallic mine.

6 Conclusions

(1) A 3D natural source EM inversion method was proposed based on an efficient MG solver. The MG solver is applied to solving both the forward and adjoint equations. The LU decomposition used in the MG algorithm for one-mode forward modeling can be reused for the other mode and their adjoint computations.

(2) A synthetic model with six boxes was used for both forward modeling and inversion tests. The numerical results for the model show that the algorithm improves the inversion efficiency by 3.8 times compared to ModEM.

(3) The application of the inversion algorithm for real data inversion shows that our algorithm is effective and stable for real application. The study provides a valuable reference for delineating metal deposits using EM methods.

CRediT authorship contribution statement

Yong-fei WANG: Conceptualization, Methodology, Software, Visualization, Writing − Original draft, Review & editing; **Rong-wen GUO:** Conceptualization, Funding acquisition, Supervision; **Zhuo LIU:** Conceptualization, Investigation, Methodology, Visualization; **Ding-hui YANG:** Supervision; **Deng-kang WANG:** Writing − Review & editing.

Declaration of competing interest

The authors declare that they have no known competing financial interests or personal relationships that could have appeared to influence the work reported in this paper.

Acknowledgments

This work was financially supported by the National Science and Technology Major Project, China (No. 2024ZD1002100), the National Natural Science Foundation of China (Nos. 42330801, 42474112, 42504062), the China Postdoctoral Science Foundation (No. 2024M761704) and Shuimu Tsinghua Scholar Program of Tsinghua University, China (No. 2024SM114).

References

[1] XIE Jing, CUI Yi-an, LIU Jian-xin, GUO You-jun, ZHANG Li-juan, LUO Yi-jian, ZHANG Peng-fei. A review on theory, modeling, inversion, and application of self-potential in marine mineral exploration [J]. Transactions of Nonferrous Metals Society of China, 2023, 33(4): 1214−1232.

[2] LIU Jian-xin, LIU Rong, GUO Rong-wen, TONG Xiao-zhong, XIE Wei. Research progress of electromagnetic method in nonferrous metal mineral exploration [J]. The Chinese Journal of Nonferrous Metals, 2023, 33(1): 261−284. (in Chinese)

[3] LIU Jian-xin, LIU Hui-peng, LIU Rong, XUE Jian-qiang, LI Yue-hua, WANG Fang. Application of aeromagnetic survey to mineral exploration of Jinping, Yunnan, China by using multirotor UAV [J]. Transactions of Nonferrous Metals Society of China, 2023, 33(5): 1550−1558.

[4] SIRIPUNVARAPORN W. Three-dimensional magneto-telluric inversion: an introductory guide for developers and users [J]. Surveys in Geophysics, 2012, 33: 5−27.

[5] PATRO P K. Magnetotelluric studies for hydrocarbon and geothermal resources: Examples from the Asian region [J]. Surveys in Geophysics, 2017, 38: 1005−1041.

[6] ZHANG Li-juan, CUI Yi-an, XIE Jing, LIU Jian-xin. 3D inversion imaging of self-potential current source induced by mineral polarization [J]. Transactions of Nonferrous Metals Society of China, 2025, 35(3): 945−953.

[7] XUE Jian-qiang, LIU Jian-xin, HUANG De-zhi, ZHOU Wei-jian, LIU Chun-ming, CAO Yu-sen, CAO Chuang-hua. Sources of rare earth elements REE+Y (REY) in Bayili Coal Mine from Wensu County of Xinjiang, China [J]. Transactions of Nonferrous Metals Society of China, 2021, 31(10): 3105−3115.

[8] WANG Y F, LIU J X, GUO R W. Efficient multigrid algorithms for three-dimensional electromagnetic forward modeling [J]. Surveys in Geophysics, 2025, 46: 555−593.

[9] CHEN C J, KRUGLYAKOV M, KUVSHINOV A. Advanced three-dimensional electromagnetic modelling using a nested integral equation approach [J]. Geophysical Journal International, 2021, 226(1): 114−130.

[10] CAI H Z, XIONG B, HAN M R, ZHDANOV M. 3D controlled-source electromagnetic modeling in anisotropic medium using edge-based finite element method [J]. Computers and Geosciences, 2014, 73: 164−176.

[11] CHEN H, REN Z Y, TANG J T. Magnetotelluric adaptive inversion using multi-resolution tetrahedral grids: Application to the North China craton [J]. Journal of Geophysical Research: Solid Earth, 2025, 130: e2024JB030405.

[12] QIN C, ZHAO N, WANG X B, LI H. An hp-adaptive finite-element approach for 3D controlled-source electromagnetic forward modeling [J]. Geophysics, 2025, 90(3): WA87−WA101.

[13] PENG R H, HAN B, LIU Y J, HU X Y. EM3DANI: A Julia package for fully anisotropic 3D forward modeling of electromagnetic data [J]. Geophysics, 2021, 86(5): F49−F60.

[14] HU Y, YANG D K, LI Y C, WANG Z G, LU Y. 3-D numerical study on controlled source electromagnetic monitoring of hydraulic fracturing fluid with the effect of steel-cased wells

[J]. IEEE Transactions on Geoscience and Remote Sensing, 2022, 60: 1−10.

[15] EGBERT G D, KELBERT A. Computational recipes for electromagnetic inverse problems [J]. Geophysical Journal International, 2012, 189(1): 251−267.

[16] ZHOU J J, BAI N B, HAN B, HU X Y, XIAO T J, HUANG G S, LI J P. Gauss−Newton with preconditioned conjugate gradient magnetotelluric inversion for 3-D axial anisotropic conductivities [J]. IEEE Transactions on Geoscience and Remote Sensing, 2024, 62: 1−14.

[17] HU X Y, BAI N B, HAN B, PENG R H, ZHOU J J, ZHU D, HUANG G S. A 3D inversion algorithm of magnetotelluric data based on the solution space dimensionality reduction technique [J]. Geophysics, 2025, 90(3): E91−E104.

[18] SU Y, WANG L Y, YIN C C, HUANG X Y, LIU Y H, REN X Y, ZHANG B, BARANWAL V C. 3-D Airborne EM inversion based on multiscale correlation in Shearlet domain [J]. IEEE Transactions on Geoscience and Remote Sensing, 2024, 62: 1−12.

[19] SIRIPUNVARAPORN W, UYESHIMA M, EGBERT G D. Three dimensional inversion for Network-Magnetotelluric data [J]. Earth, Planets and Space, 2004, 56: 893−902.

[20] NEWMAN G A, BOGGS P T. Solution accelerators for large-scale three-dimensional electromagnetic inverse problems [J]. Inverse Problems, 2004, 20(6): S151−S170.

[21] LIU Z G, REN Z Y, YAO H B, TANG J T, LU X S, FARQUHARSON C G. A parallel adaptive finite-element approach for 3-D realistic controlled source electromagnetic problems using hierarchical tetrahedral grids [J]. Geophysical Journal International, 2023, 232: 1866−1885.

[22] NEWMAN G A, ALUMBAUGH D L. Three-dimensional magnetotelluric inversion using non-linear conjugate gradients [J]. Geophysical Journal International, 2000, 140(2): 410−424.

[23] LI J, LIU J X, OGAWA Y, GUO R W, WANG X L, WANG Y F, ZHOU K K, XU J D. Three-dimensional magnetotelluric inversion using an adaptive algebraic multi-resolution sampling approach [J]. Geophysics, 2025, 90(6): E225−E239.

[24] YANG Ding-hui, DONG Xing-peng, HUANG Jian-dong, FANG Zhi-long, HUANG Xue-yuan, LIU Shao-lin, LIU Meng-xue, MENG Wei-juan. High-resolution full waveform seismic imaging: Progresses, challenges, and prospects [J]. Science China Earth Sciences, 2025, 68: 315−342.

[25] RODI W, MACKIE R L. Nonlinear conjugate gradients algorithm for 2-D magnetotelluric inversion [J]. Geophysics, 2001, 66(1): 174−187.

[26] CAI H Z, LONG Z D, LIN W L, LI J H, LIN P R, HU X Y. 3D multinary inversion of controlled-source electromagnetic data based on the finite-element method with unstructured mesh [J]. Geophysics, 2021, 86(1): E77−E92.

[27] WANG X Y, CAI H Z, HU X Y, LIU L C, LIU S, LI J H, HUANG Q, CHENG S J. Three-dimensional magnetotelluric inversion with sub-domain decomposition and zero-order minimum entropy constraint [J]. Geophysics, 2025, 90(5), E191−E208.

[28] MOORKAMP M, HEINCKE B, JEGEN M, ROBERTS A W, HOBBS R W. A framework for 3-D joint inversion of MT, gravity and seismic refraction data [J]. Geophysical Journal International, 2011, 184(1): 477−493.

[29] SIRIPUNVARAPORN W, EGBERT G D. WSINV3DMT: Vertical magnetic field transfer function inversion and parallel implementation [J]. Physics of the Earth and Planetary Interiors, 2009, 173(3/4): 317−329.

[30] SINGH A, DEHIYA R, GUPTA P K. A MATLAB based 3D modeling and inversion code for MT data [J]. Computers & Geosciences, 2017, 104: 1−11.

[31] VARILSÜHA D. 3D inversion of magnetotelluric data by using a hybrid forward-modeling approach and mesh decoupling [J]. Geophysics, 2020, 85(5): E191−E205.

[32] KELBERT A, MEQBEL N, EGBERT G D, TANDON K. ModEM: A modular system for inversion of electromagnetic geophysical data [J]. Computers & Geosciences, 2014, 66: 40−53.

[33] YU N, WANG E C, WANG X B, KONG W X, LI D W, LI R H. The influence of the Ailaoshan-Red River shear zone on the mineralization of the Beiya deposit on the southeastern margin of the Tibetan Plateau revealed by a 3-D magnetotelluric survey [J]. Journal of Geophysical Research: Solid Earth, 2022, 127: e2021JB022923.

[34] ANSARI S M, FARQUHARSON C G, MACLACHLAN S P. A gauged finite-element potential formulation for accurate inductive and galvanic modelling of 3-D electromagnetic problems [J]. Geophysical Journal International, 2017, 210(1): 105−129.

[35] TANG W W, LI Y G, LIU J X, DENG J Z. Three-dimensional controlled-source electromagnetic forward modeling by edge-based finite element with a divergence correction [J]. Geophysics, 2021, 86(6): E367−E382.

[36] LI J, GUO R W, LIU J X, WANG Y F, WANG X L. An efficient algebraic multi-resolution sampling approach to 3-D magnetotelluric modelling [J]. Geophysical Journal International, 2023, 235(1): 166−177.

[37] DONG H, EGBERT G D. Divergence-free solutions to electromagnetic forward and adjoint problems: A regularization approach [J]. Geophysical Journal International, 2019, 216(2): 906−918.

[38] WANG Y F, GUO R W, LIU J X, LI J, LIU R, CHEN H, CAO X, YIN Z H, CAO C H. A divergence free vector finite element method for efficient 3D magnetotelluric forward modeling [J]. Geophysics, 2024, 89(1): E1−E11.

[39] XIAO T J, HUANG X Y, WANG Y. Three-dimensional magnetotelluric modelling in anisotropic media using the A-phi method [J]. Exploration Geophysics, 2019, 50(1): 31−41.

[40] WANG Y F, LIU J X, EGBERT G D, GUO R W, LI J, YANG G Q, TIAN S Q, CHEN H. Multicolor-MG: An efficient parallel multigrid code based on multi-color block-wise Gauss Seidel smoothers for 3D natural source electromagnetic forward modeling[J]. Geophysics, 2025, 90(4): F43−F52.

[41] LI G, ZHANG L L, HAN B. Stable electromagnetic modeling using a multigrid solver on stretching grids: the magnetotelluric example [J]. IEEE Geoscience and Remote Sensing Letters, 2016, 13(3): 334−338.

[42] GUO R W, WANG Y F, EGBERT G D, LIU J X, LIU R, PAN K J, LI J, CHEN H. An efficient multigrid solver based on a four-color cell-block Gauss-Seidel smoother for 3D Magnetotelluric forward modeling [J]. Geophysics, 2022, 87(3): E121−E133.

[43] HUANG X Y, YIN C C, WANG L Y, LIU Y H, ZHANG B, REN X Y, SU Y, LI J, CHEN H. A geometric multigrid method for 3D magnetotelluric forward modeling using finite-element method [J]. Remote Sensing, 2023, 15(2): 537.
[44] PAN K J, WANG J X, LIU Z G, OU Z Y, GUO R W, REN Z Y. An efficient cascadic multigrid method with regularization technique for 3D electromagnetic finite-element anisotropic modeling [J]. Geophysics, 2024, 89(6): E241−E253.
[45] WANG Y F, LIU J X, GUO R W, PAN K J, YANG G Q, LI J. A robust and scalable multigrid solver for 3D low-frequency electromagnetic diffusion problems [J]. IEEE Transactions on Geoscience and Remote Sensing, 2024, 62: 1−9.
[46] WANG Y F, LIU J X, GUO R W, LIU R, LI J, CHEN H, YANG G Q. Efficient three-dimensional magnetotelluric forward modeling based on a geometric multigrid preconditioner [J]. Chinese Journal of Geophysics, 2022, 65(5): 1839−1852. (in Chinese)
[47] KONG W X, TAN H D, LIN C H, UNSWORTH M, LEE B, PENG M, WANG M, TONG T. Three-dimensional inversion of magnetotelluric data for a resistivity model with arbitrary anisotropy [J]. Journal of Geophysical Research: Solid Earth, 2021, 126: e2020JB020562.
[48] DENG J, WANG Q F, GAO L, HE W Y, YANG Z Y, ZHANG S H, CHANG L J, LI G J, SUN X, ZHOU D Q. Differential crustal rotation and its control on giant ore clusters along the eastern margin of Tibet [J]. Geology, 2021, 49(4): 428−432.
[49] MAO J W, ZHOU Y M, LIU H, ZHANG C Q, FU D G, LIU B. Metallogenic setting and ore genetic model for the Beiya porphyry-skarn polymetallic Au orefield, western Yunnan, China [J]. Ore Geology Reviews, 2017, 86: 21−34.
[50] LI W C, WANG J H, HE Z H, DOU S. Formation of Au-polymetallic ore deposits in alkaline porphyries at Beiya, Yunnan, Southwest China [J]. Ore Geology Reviews, 2016, 73(2): 241−252.
[51] HOU Z Q, ZHOU Y, WANG R, ZHENG Y C, HE W Y, ZHAO M, EVANS N J, WEINBERG R F. Recycling of metal-fertilized lower continental crust: Origin of non-arc Au-rich porphyry deposits at cratonic edges [J]. Geology, 2017, 45(6): 563−566.
[52] CALDWELL T G, BIBBY H M, BROWN C. The magneto-telluric phase tensor [J]. Geophysical Journal International, 2004, 158(2): 457−469.

基于高效多重网格法的金属矿电磁数据三维反演

王永斐[1]，郭荣文[2,3,4,5]，柳 卓[6]，杨顶辉[1]，王登康[2,3,4,5]

1. 清华大学 数学科学系，北京 100084；
2. 中南大学 关键矿产研究与勘探国家重点实验室，长沙 410083；
3. 中南大学 地球科学与信息物理学院，长沙 410083；
4. 湖南省有色资源与地质灾害探测重点实验室，长沙 410083；
5. 中南大学 有色金属或矿预测与地质环境监测教育部重点实验室，长沙 410083；
6. Doerr School of Sustainability, Department of Earth and Planetary Sciences, Stanford University, Stanford, California 94305, USA

摘 要：提出一种基于双色平面 Gauss−Seidel(GS)多重网格(MG)正演求解器的非线性共轭梯度(NLCG)法的三维电磁反演算法，以提高反演效率。结果表明，利用所提出的高效 MG 求解器可使单次反演计算效率提升约 3 倍。首先，通过对一个合成模型的测试验证 MG 求解器的精度；随后，利用该模型评估反演算法的数值性能；最后，将反演算法应用于北崖多金属矿区野外电磁数据集的实测电磁数据，获得三维电阻率模型并分析金属矿床的形成过程。

关键词：金属矿物；电磁数据；梯度反演法；多重网格求解器

(Edited by Bing YANG)